



Mechanical activation of TiO₂/Fe₂O₃ nanocomposite for arsenic adsorption: effect of ball-to-powder ratio and milling time

Mercyrani Babudurai¹ · Onyekachi Nwakanma² · Araceli Romero-Nuñez² · Ravichandran Manisekaran³ · Velumani Subramaniam^{1,2} · Homero Castaneda⁴ · Anish Jantrania⁵

Received: 2 November 2020 / Accepted: 8 January 2021 / Published online: 9 February 2021
© Islamic Azad University 2021, corrected publication 2021

Abstract

Arsenic contamination and its removal from the ground or natural water become an inevitable research line as it is highly carcinogenic and toxic. In the last few decades, nanotechnology has been achieved to provide accessible clean water for all living organisms. In this work, the various ratios of TiO₂/γ-Fe₂O₃ nanocomposite (T/M NCs) synthesized using the ball-milling route serve as nano-adsorbent for removing arsenic species. This study presents a non-toxic, low-cost, and easily accessible method for synthesizing NCs in large quantities for adsorption, offering promising results for arsenic removal from water. The ball-milling synthesis provides a comparatively, cost-effective strategy and for modulating the properties of nanostructured materials. The milling time and ball-to-powder ratio variations allow modifying the T/M NCs properties during the synthesis. The structural, morphological, and optical characterizations using X-ray diffraction, high-resolution electron microscopy, and UV–Vis analysis showed the formation of predominantly spherical-shaped anatase TiO₂ and cubic γ-Fe₂O₃ with varying bandgap between 2.06 and 2.14 eV, which changes because of the nanomaterial phase transformation during the milling process. Elemental compositional analysis using EDS showed the uniform distribution of Ti and Fe atoms. The vibrational modes observed using Raman spectroscopy confirmed the presence of anatase TiO₂ and γ-Fe₂O₃ within the NCs and showed the associated variations with changes in synthesis parameters. X-ray photoelectron spectroscopy analysis of the synthesized ratios indicated a variation in the binding energy (ΔBE) and the evidence of charge transfer in between TiO₂ and γ-Fe₂O₃ NCs. The adsorption studies using the various T/M NCs ratios show varying performances. The enhanced performances obtained for the NC of anatase TiO₂ and γ-Fe₂O₃ with the most intense phase peak ratio ($I_{(101)}/I_{(311)}$) of 1.2

✉ Velumani Subramaniam
velu@cinvestav.mx

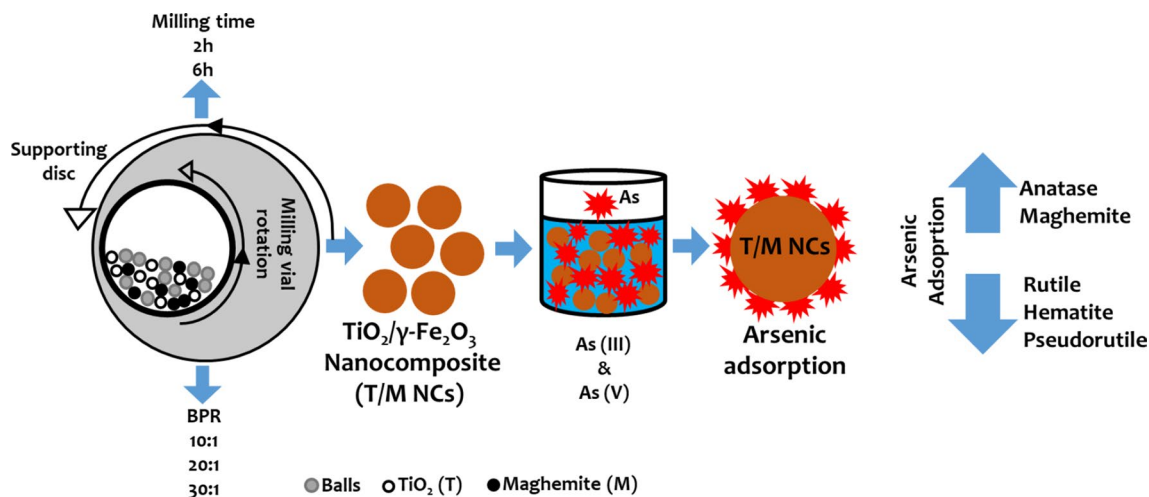
- ¹ Nanoscience and Nanotechnology Program, Centro de Investigación y de Estudios Avanzados del Instituto Politécnico Nacional (CINVESTAV-IPN), Av. Instituto Politécnico Nacional 2508, Col. San Pedro Zacatenco, Ciudad de México 07360, Mexico
- ² Department of Electrical Engineering (SEES), Centro de Investigación y de Estudios Avanzados del Instituto Politécnico Nacional (CINVESTAV-IPN), Av. Instituto Politécnico Nacional 2508, Col. San Pedro Zacatenco, 07360 Ciudad de México, Mexico
- ³ Laboratorio de Investigación Interdisciplinaria, Área de Nanoestructuras y Biomateriales, Escuela Nacional de Estudios Superiores Unidad León; Universidad Nacional Autónoma de México, León, Guanajuato, Mexico
- ⁴ Department of Materials Science and Engineering, Texas A&M University, College Station, TX 77843, USA
- ⁵ Department of Biological and Agricultural Engineering, Agrilife Extension, Texas A&M University, College Station, TX 77843, USA



and above shows decreased adsorption efficiency with the phase changes into rutile TiO_2 , hematite, and pseudorutile phases. The elimination of As(III) and As(V) using the synthesized NCs confirms that the ball milling technique can produce nano-materials with desirable properties for adsorption purposes.

Graphic abstract

The effect of BPR and milling time on $\text{TiO}_2/\gamma\text{-Fe}_2\text{O}_3$ nanocomposite (T/M NCs) and its impact on Arsenic adsorption.



Keywords Ball milling · Arsenic · Nano-adsorbent · $\text{TiO}_2/\gamma\text{-Fe}_2\text{O}_3$ nanocomposite

Introduction

Access to safe drinking water is a critical aspect of protecting public health. Nonetheless, recent studies disclose that more than 230 million people worldwide are affected by arsenic-contaminated drinking water [1]. Arsenic is a crystalline "metalloid," a natural element that ranks the 20th most occurring element in the earth's crust. Arsenic (As) exists in various oxidation states (− III, 0, + III, + V), but Arsenite(III) and Arsenate(V) are mostly present in an aqueous medium [2]. These can be leached from industrial wastes, biological activity, soils, mining activities, and fertilizers, containing minerals and occurring naturally [3]. The long-term exposure or intake of As-contaminated food or water will lead to many serious diseases; acute and chronic poisoning involves respiratory, gastro-intestinal, conjunctivitis, hyperkeratosis, hyperpigmentation, cardiovascular diseases, disturbance in the peripheral vascular and nervous systems. It is also highly carcinogenic, leading to cause cancer in the lungs, bladder, liver, renal, and skin cancer [4]. Therefore, there is a significant need to remove it from drinking water and food materials, thereby avoiding its adverse effects to protect humanity [5].

Arsenic can be eliminated from drinking water by numerous methods, including reverse osmosis, adsorption, chemical treatment, membrane filtration, ion exchange, electrochemical treatment, and co-precipitation [6–9]. Among the

removal techniques, the most common method employed, especially for aqueous solutions, is adsorption due to its advantages, including high removal efficiency, simplicity, easy operation, wide pH range, and less harmful by-products low-cost [2, 10]. As pollutants widely affect developing countries, the treatment technique must be cost-effective and easy to operate. Most adsorbents used for arsenic removal include carbon-based materials, surfactants, agriculture, industrial wastes, and polymers. Also, some metals and metal oxides, including $\gamma\text{-Fe}_2\text{O}_3$, TiO_2 , CeO_2 , CuO , ZrO_2 , have been extensively employed in aqueous media considering the low-cost, high adsorption capacity and affinity towards arsenic [6, 11, 12]. To enhance the adsorption behavior, two or more metal oxides combined have attracted considerable attention and have attracted tremendous interest from researchers recently [13–15].

The common arsenic contaminants exist mainly in either of the forms; arsenic(III) or arsenic(V). Studies show that it is easier to remove the oxidized form of As(V) in comparison to the reduced form of As(III), which is challenging to eliminate because of the speciation at different pH. The As(III) mainly occurs in uncharged arsenous acid H_3AsO_3 , under reducing conditions at pH 6.5–8.5, and neutral in most other pH ranges. In contrast, As(V) is present in the form of H_2AsO_4^- and HAsO_4^{2-} anions in oxidizing waters [16], so designing a nano-adsorbent combining two or more metal oxides can also aid in the efficient removal of As(III).



The arsenic presence in the environment, especially in water bodies, comes from arsenic-bearing minerals and the reductive dissolution of As(V) to the much more soluble As(III). Both As(III) and As(V) anions are toxic, with the As(III) being more toxic, very soluble, and mobile in water environments. As(V) occurs in more stable aerobic or oxidizing conditions such as surface waters, while As(III) compounds are stable under anaerobic or mildly reducing conditions such as subsurface waters. A primary method of arsenic removal, especially from water, is surface complexation of As(III) and As(V) with solid sorbents, e.g., containing titanium and iron. For instance, Fe reacts with As anions and can form insoluble and eventually very stable Fe–As complexes that remove As from water [17, 18].

The anatase TiO₂ phase, among various metal oxides, is widely employed to remove arsenic contaminants due to its low toxicity, physicochemical stability, facile preparation, low cost, and eco-friendly [19]. However, it has certain limitations posing a significant drawback, such as the surface area, which decreases due to agglomeration, removed by forming nanocomposites or coating with other metals or metal oxides [20]. Also, the separation of the adsorbed materials tends to be problematic with only TiO₂ nanomaterials in the aqueous media. Combining the TiO₂ nanomaterials with other nanomaterials, e.g., iron-based adsorbents, eliminate these common challenges. The iron-based adsorbents play a significant role in adsorption due to their ion-exchange and specific adsorption to hydroxyl groups. Importantly, they help recover and recycle the nanoparticles because of their magnetic property after arsenic adsorption [21, 22]. Hence, one of the most suitable iron-oxide adsorbents is the maghemite (γ -Fe₂O₃), which is more stable than magnetite (Fe₃O₄) combined with TiO₂ anatase, to overcome the limitation of TiO₂ and also to increase the efficiency of As(III) and (V) adsorption.

Several top-down (e.g., ball milling, laser ablation, ion sputtering) and bottom-up techniques (e.g., physical and chemical vapor deposition, hydro and solvothermal methods, sol–gel, pyrolysis, microwave, and biological methods) offer means of synthesizing nanomaterials for adsorption purposes [23]. However, the ball milling method provides an effective mechanical milling process with several advantages over the other synthesis methods preparing NCs, especially the cost-to-efficiency ratios. This process does not require any solvents. Other advantages include the relatively low installation cost, low power and grinding medium, suitability for both batch and continuous operation, and capability to treat various degrees of materials hardness. The ball-milling process has also gained high importance over synthesis methods because of its greener and facile technique. Hence, it eliminates waste generation from multi-step procedures, high temperature, and pressure conditions, and requires no hazardous and expensive chemicals. Also, it yields a more

considerable amount of desired product with short processing time at ambient conditions and is better suitable for large-scale industrial production [24–27]. During milling, the balls constriction provides the required friction to produce fine nanomaterials, and the generated heat contributes effectively to the reaction, essentially resulting in a reactive milling process. The process effectiveness depends on several factors, including the ball to powder ratio (BPR) and milling time, determining the properties of the synthesized nanostructures.

Considering the several advantages of ball-milling methods and the importance of NCs, especially for adsorption purposes, the current study proposes a novel method for the synthesis of anatase TiO₂ and maghemite (T/M) NCs using ball milling. The study reports optimized ball-milling parameters, including the ball-to-powder ratio (BPR) and milling time, affecting NCs properties. For instance, milling parameters and associated heat generated due to constriction affect the phases and properties of synthesized NCs, impacting adsorption. This study's results have not been reported in any previous literature to the best of our knowledge. Adsorption studies using the synthesized NCs showed desirable results for As(III) and (V) removal.

Experiments

Materials

All the chemicals utilized in this study are of analytical grade and purchased from Sigma-Aldrich, Mexico, and used without further purification. The chemicals used for the synthesis include iron(III) chloride hexahydrate (FeCl₃·6H₂O, ≥ 98%), iron(II) chloride tetrahydrate (FeCl₂·4H₂O, ≥ 99.0%), ammonium hydroxide (NH₄OH, 28–30% NH₃ basis), reagent alcohol (C₂H₅O_H), titanium chloride, (TiCl₄ 99.9%), arsenic(III) oxide (As₂O₃, ≥ 99.0%), sodium arsenate dibasic heptahydrate (HAsNa₂O₄·7H₂O, ≥ 98.0%), ammonium molybdate tetrahydrate (H₂₄MO₇N₈O₂₄·4H₂O, 99.98%), potassium antimonyl tartrate trihydrate (C₈H₄K₂O₁₂Sb₂·3H₂O, ≥ 99%), potassium permanganate (KMnO₄, ≥ 99%), sodium hydroxide (NaOH, ≥ 98%), L-ascorbic acid (C₆H₈O₆), sulphuric acid (H₂SO₄), hydrochloric acid (HCl), and acetic acid (CH₃COOH), and deionized water used for all the experiment.

TiO₂ anatase and γ -Fe₂O₃ synthesis

The TiO₂ anatase was obtained by adding 5 mL of TiCl₄ dropwise to 15 mL of ethanol at 60 °C under continuous stirring. A large amount of HCl gas released during the mixing process was safely extracted using the laboratory fume exhaust. After 30 min, a light-yellow gel was obtained, kept



in the oven at 70 °C for 24 h. The dry-gel precursor was calcined at 450 °C in the furnace (Thermo Scientific, Lindberg/Blue M VO914) and ground to obtain the TiO₂ powder [28].

The γ -Fe₂O₃ was obtained by mixing FeCl₂·4H₂O and FeCl₃·6H₂O in a 1:2 molar ratio in 100 mL of deionized water at room temperature. After proper mixing, NH₄OH solution was added dropwise to the mixture under continuous stirring with a constant nitrogen (N₂) flow until the formation of a black precipitate. The precipitate is then recovered and washed several times with deionized water until the pH becomes 7. The precipitate and suspended magnetite nanoparticles collected with the help of a strong neodymium magnet were dried in an oven (Thermo Scientific, HERA THERM) at 70 °C overnight [29]. Finally, the obtained magnetite was dried in a muffle furnace at 150 °C for 2 h to obtain a pure and stable maghemite phase.

Ball-milling process of NCs

The T/M NCs were synthesized by varying BPR (10:1, 20:1 and 30:1) and different milling times (2 and 6 h) by mixing appropriate quantities of TiO₂ and γ -Fe₂O₃ and processed using a planetary Ball Mill, MA-type PM400, Retsch with constant RPM of 300.

Spectrophotometric determination of As(III) and (V) in water samples

The spectrophotometric methods offer an alternative to conventional techniques in determining accurately and with sufficient sensitivity to the arsenic species at the trace levels in water [30]. In comparison, the method is cost-effective and may not require specialized personnel to make the measurements [31, 32].

A standard solution consisting of 100 mL of 1000 ppm, As(III) and (V), was prepared by dissolving 0.1302 g of As₂O₃, 1 g of NaOH, and 20 mL of conc. HCl in deionized water and 0.4245 g of HAsNa₂O₄·7H₂O in deionized water, respectively. After that, 2 ppm arsenic was prepared using the standard solution. Ammonium molybdate tetrahydrate solution was prepared by mixing 6.5 g of H₂₄MO₇N₈O₂₄·4H₂O in 50 mL deionized water (labeled part 1), and potassium antimonyl tartrate trihydrate solution prepared by mixing 0.175 g C₈H₄K₂O₁₂Sb₂·3H₂O of in 50 mL deionized water (labeled part 2).

Solution **A** was prepared by mixing 5 mL of part 1 solution and 5 mL of part 2 solution, and 15 mL of 9 M H₂SO₄, and solution **B** prepared by dissolving 1 g of ascorbic acid in 10 mL of deionized water, with 0.1 M of the KMnO₄ solution for the experiment. 0.1 M NaOH and acetic acid solutions were used to adjust the pH to 7. For arsenic(III) determination, 200 μ L of solution **A** and 100 μ L of solution **B** with 700 μ L H₂O were added to 4 mL of the sample

solution. Furthermore, for As(V) determination, 100 μ L of KMnO₄ solution was added to the 4 mL sample solution; after 5 min, 200 μ L of solution **A**, 100 μ L of solution **B**, and 600 μ L of H₂O added to 4 mL of the sample solution. After 2 h, absorbance is measured at 870 nm in the spectrophotometer against the reagent blank.

Adsorption studies

Batch adsorption experiments with doublets were performed to remove As(III) and (V) under the following conditions: concentration = 2 ppm, pH 7, adsorbent dosage = 0.5 g/L, RPM = 300, and room temperature. T/M NCs obtained with the BPR mentioned above (10:1, 20:1, and 30:1) and (2 and 6 h) milling time were used to adsorb As(III) and (V). A total of 8 samples were used; TiO₂ (T), γ -Fe₂O₃ (M), T/M NCs—10:1, 20:1, and 30:1 with BPR of 2 and 6 h. The 1:1 ratio was maintained for the preparation of 6 nanocomposites.

Characterization

Using Bruker D2-phasex X-ray diffractometer (Cu_{K α} λ = 1.5406 Å) in the range from 10° to 80°, the structural properties of the synthesized TiO₂, γ -Fe₂O₃, and the nanocomposites were analyzed using X-ray diffraction to identify the phases and the crystallite properties of the nanostructures. The crystallite size (D_p) of the samples were calculated using the Scherrer equation:

$$D_p = \frac{K\lambda}{\beta \cos\theta}, \quad (1)$$

K is the shape factor (0.94, assuming spherical crystallites), and β is the full width at half maximum (FWHM), while θ is the Bragg's diffraction angle.

The interplanar distance, d , measured using the equation

$$d = \frac{n\lambda}{2 \sin\theta}, \quad (2)$$

allows for calculating the lattice parameters (a , c) for tetragonal structure using the relation

$$\frac{1}{d^2} = \frac{h^2 + k^2}{a^2} + \frac{l^2}{c^2}, \quad (3)$$

and cubic structure using the relation

$$\frac{1}{d^2} = \frac{h^2 + k^2 + l^2}{a^2}, \quad (4)$$

hkl is the miller indices from the X-ray diffractogram.

The dislocation density, δ , measuring the number of dislocation lines in a unit area, is calculated using the relation

$$\delta = \frac{1}{D_p^2}, \quad (5)$$

and the microstrain was calculated by the following equation [33]:

$$\varepsilon = \frac{\beta}{4 \tan \theta}. \quad (6)$$

High-resolution transmission electron microscopy (HRTEM) at 200 keV using JEM—2010, JEOL Inc for studying the morphology of the synthesized nanomaterials. The morphological studies and micrographs were obtained using TESCAN VEGA scanning electron microscope (SEM) at 25× magnification, equipped with energy-dispersive X-ray spectroscopy (EDS) for the elemental compositional analysis. Raman characterizations using the NT-MDT INTEGRA system helped identify the phases and vibrational modes of the synthesized materials. X-ray photoelectron spectroscopy (XPS) using scanning XPS microprobe PHI 5000 VersaProbe II (Al X-ray source: 1486.6 eV) allows for characterizing the binding energy of the materials. The reflectance measurements in the wavelength of 200–800 nm using JascoV-670 spectrophotometer coupled with the integrating sphere for the bandgap measurement allowed for bandgap estimations of the samples. The bandgap of the materials calculated using Kubelka–Munk function is given by [34]

$$F(R) = \frac{(1 - R)^2}{2R}. \quad (7)$$

The extrapolation of the plot $(F(R) \cdot hv)^2$ vs. hv to the horizontal axis (where R is the reflectance), considering an indirect transition of the materials, allows for the estimation of the energy bandgap value from the Kubelka–Munk theory. We calculated the percentage (%) removal of the contaminants using the relation:

$$\% \text{Removal} = \left| \frac{C_i - C_f}{C_i} \right| \times 100, \quad (8)$$

C_i and C_f are the contaminants' initial and final concentrations, in this study being As(III) and (V).

Results and discussion

XRD diffractograms

The structural analysis using X-ray diffractograms confirmed the successful synthesis of tetragonal TiO₂ anatase structure through the sol–gel method and cubic spinel γ -Fe₂O₃ structure synthesized through co-precipitation method, with no secondary or intermediate phases (Fig. 1). A comparison of the lattice parameters of the synthesized nanostructures

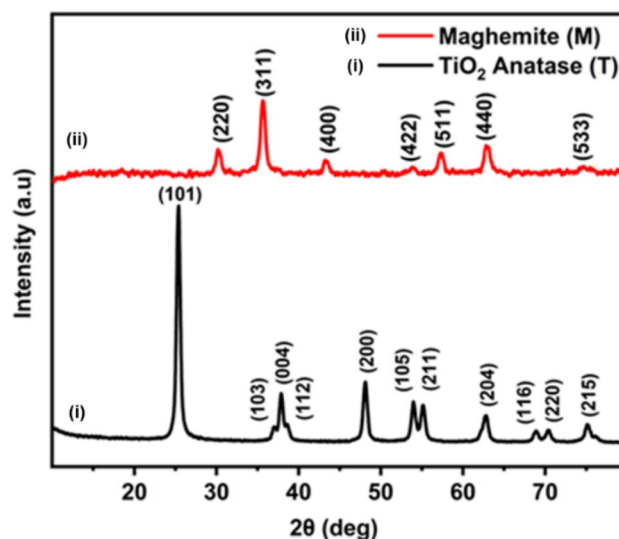


Fig. 1 X-ray diffractograms of anatase (TiO₂) and maghemite spinel cubic (γ -Fe₂O₃) structures obtained by sol–gel and co-precipitation method, respectively

was calculated using Eqs. (2)–(4) in Sect. 1, with ICDD reference (no. 00-064-0863-anatase), 00-039-1346-maghemite). Table 1 represents the comparable lattice parameters between the synthesized nanostructures and the referenced materials. We estimated the average crystallite size of TiO₂ and γ -Fe₂O₃ nanomaterials using Eq. (1) presented in Table 2 and calculated the associated dislocation density (δ) estimated from the D_p (Eq. 4) and strain (Eq. 5). The calculated dislocation densities and the microstrain of the synthesized nanomaterials showed comparative values to reported literature for the nanomaterials, which may be due to some interatomic diffusion that modifies the atomic (e.g., oxygen) contents of the structure [35].

The synthesized TiO₂ and γ -Fe₂O₃ were processed by ball milling with varying parameters like milling time and BPR. Composite of T/M NCs with BPR 10:1 milled for 2 h (Fig. 2a) shows the prominent peaks corresponds to TiO₂ anatase and γ -Fe₂O₃ maghemite phases. Increasing the BPR (20:1) creates more friction between the balls, generating more heat reaction during the milling [36]. This heat accounts for the decrease of the TiO₂ anatase peak and transformation of the γ -Fe₂O₃ to hematite (Fe₂O₃) and pseudorutile phases. Further increase in the BPR (30:1) presumably generates more heat and friction, resulting in the further decrement of the TiO₂ anatase peak and cause the rise of the secondary phases (hematite and pseudorutile).

Milling for 6 h with the BPR of 10:1 showed similar results than their counterpart at 2 h in terms of TiO₂ phases, but with slightly reduced peak intensities, attributed to the heat generated over a longer duration from attrition (Fig. 2b). Increasing the BPR (20:1) for 6 h shows a higher



Table 1 Comparison of the lattice parameters of synthesized TiO₂ and γ-Fe₂O₃ against the corresponding ICDD reference data

Samples	Experiment					Reference				
	2θ	d (Å)	a (Å)	c (Å)	cla	2θ	d (Å)	a (Å)	c (Å)	cla
Anatase (TiO ₂)	25.36	3.5091	3.7792	9.4872	2.5104	25.30	3.5163	3.7854	9.4937	2.7000
Maghemite (γ-Fe ₂ O ₃)	35.65	2.5161	8.3431	8.3431	1	35.66	2.517	8.3515	8.3515	1

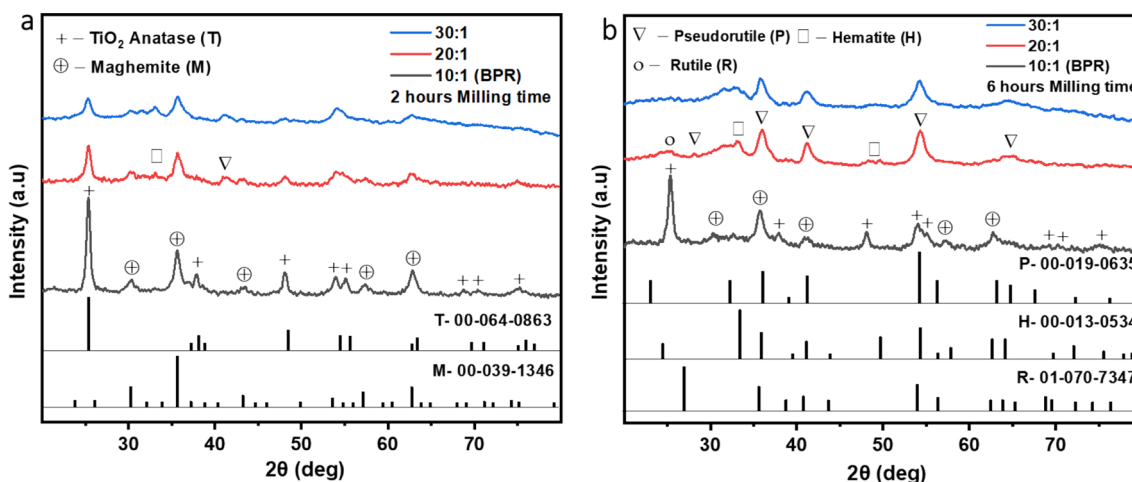
Table 2 The calculated crystallite parameters from XRD studies; crystallite sizes, dislocation densities, and strain of anatase and cubic maghemite

Samples	2θ	FWHM	Average D _p (nm)	Average δ (× 10 ⁻³ nm ⁻²)	ε × 10 ⁻³
Anatase (TiO ₂)	25.36	0.5776	14	4.81	6.51
Maghemite (γ-Fe ₂ O ₃)	35.65	0.7434	12	8.62	8.14

decay of the TiO₂ anatase phase with the appearance of the sharper and more intense peak of the pseudorutile phase along with the small shoulder peaks of the rutile phase. Similarly, the intensity of the maghemite peaks decayed, with more intense peaks of hematite appearing. These changes in the peak intensities occur due to change in phases from

anatase to pseudorutile for TiO₂ and γ-Fe₂O₃ to hematite phases when the milling time lasts longer durations at higher BPR due to attrition effects. The same behavior of phase changes appeared using increased BPR (30:1) for 6 h, in which pseudorutile and hematite phases are the most prominent ones [37].

The calculated crystallite sizes from the T/M NCs were taken from the most intense peaks corresponding to anatase (101). Results are shown in Table 3 exhibiting a slight increase in crystallite size, from BPR 10:1 to 20:1, and then a decrease in 30:1 BPR. The same behavior has occurred for 6 h milled samples. The associated strain and dislocation densities followed a similar variation pattern, decreasing and later increased. These changes in the structural phases of the synthesized composite structure may affect the adsorption process's performance. The intensity ratios for the prominent

**Fig. 2** X-ray diffractograms of TiO₂/maghemite (T/M) nanocomposite at different BPR for **a** 2 h and **b** 6 h (T TiO₂ anatase, M maghemite, H hematite, P pseudorutile, R rutile)**Table 3** The calculated crystallite parameters from XRD studies; crystallite sizes, dislocation densities, and strain for the different BPR and milling times

BPR	2 h milling					6 h milling				
	2θ (°)		Average D _p (nm)	δ (× 10 ⁻³ nm ⁻²)	ε × 10 ⁻³	2θ (°)		Average D _p (nm)	δ (× 10 ⁻³ nm ⁻²)	ε × 10 ⁻³
	TiO ₂	Fe ₂ O ₃				TiO ₂	Fe ₂ O ₃			
10:1	25.36	35.63	13	5.71	9.04	25.36	35.69	12	7.17	11.0
20:1	25.36	35.67	15	4.56	8.89	25.34	35.99	14	5.47	9.40
30:1	25.30	35.69	11	8.03	11.6	25.38	35.75	9	11.8	10.9

peaks of TiO_2 and $\gamma\text{-Fe}_2\text{O}_3$, $I_{(101)}/I_{(311)}$, Fig. 3 was calculated for all the T/M NCs synthesis. A higher fraction of anatase TiO_2 and $\gamma\text{-Fe}_2\text{O}_3$ phases above the ratio 1.2, which we observed for BPR of 10:1 for both 2 and 6 h, is determined to be more suitable for the adsorption process.

UV–Vis diffuse reflectance studies

The synthesized TiO_2 material has a bandgap of 3.2 eV, while the measured bandgap of the $\gamma\text{-Fe}_2\text{O}_3$ material is 1.95 eV, shown in Fig. 4. The wide bandgap of the TiO_2 possesses one of the limitations that affect its adsorption efficiency, due to the numerous charge transfer during adsorption mechanisms. During NCs structure formation,

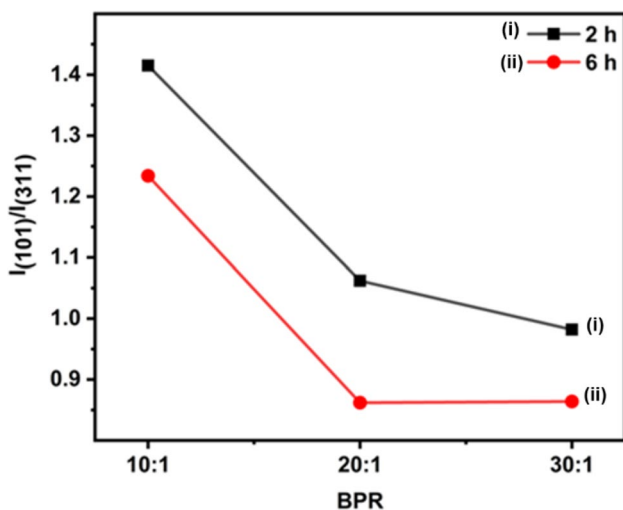


Fig. 3 A plot of the ratio of $I_{(101)}/I_{(311)}$ against the BPR for different times

the parent material receives an extra electron, leaving the donating material with more holes to balance the charge transfer and forming a type II heterostructure [38]. Therefore, the addition of maghemite to titania promotes the transfer of electrons to TiO_2 (leaving behind a compensating amount of hole) and resulting in a decrement of energy bandgap of the T/M NCs to TiO_2 [39]. In this case, an excess of electrons is generated due to composite formation and could become useful for adsorption in the sorption-ion exchange mechanism [40, 41].

The variation in band gap values for the different T/M NCs is associated with the electron transfer, as mentioned earlier, which seems to differ with the diverse phases of the NCs. The bandgaps of ratios milled for 2 and 6 h (Fig. 5a) exhibit minor variations, between 2.06 eV and 2.10 eV, respectively, being BPR 20:1 sample exhibiting the lower value. The bandgap reduction is may be due to the higher inclusion of %Fe within the nanocomposite that is evident from the EDS analysis (Table 4), even though the peak intensities are reduced while maintaining the desired phases (Fig. 2a). The bandgap for milling at a BPR of 30:1 increased to 2.10 eV, attributed to changes and the presence of secondary phases. Thus, we may allude that changes in the phases, from anatase to pseudorutile and from maghemite to hematite, causes the bandgap increment [42] as evident from the estimated bandgap of composites formed after 6 h (Fig. 5b), which increased from 2.08 eV to 2.16 eV with increasing BPR. However, we observed from the extrapolation of plots the existence of only one bandgap for each of the synthesized ratios.

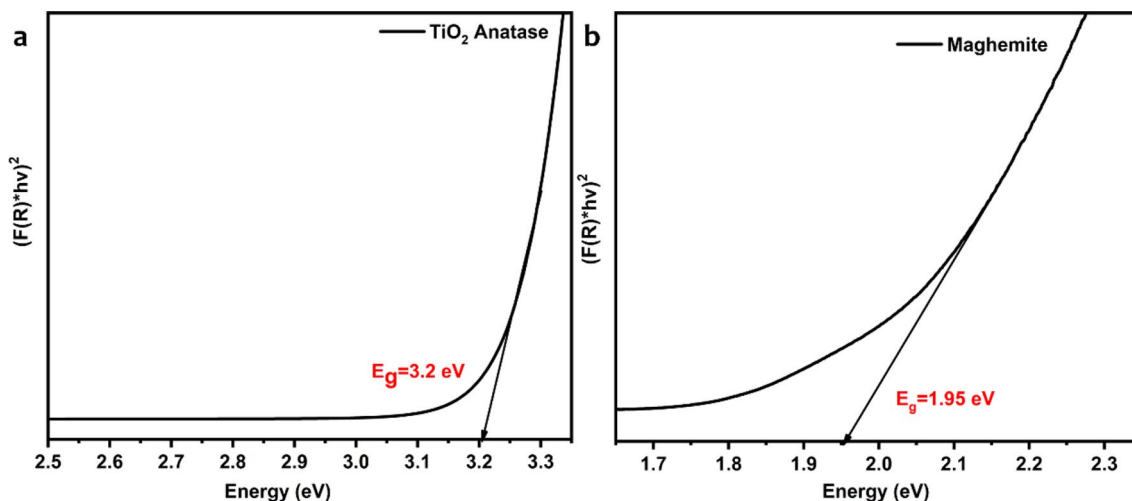


Fig. 4 The bandgap of **a** TiO_2 and **b** Maghemite



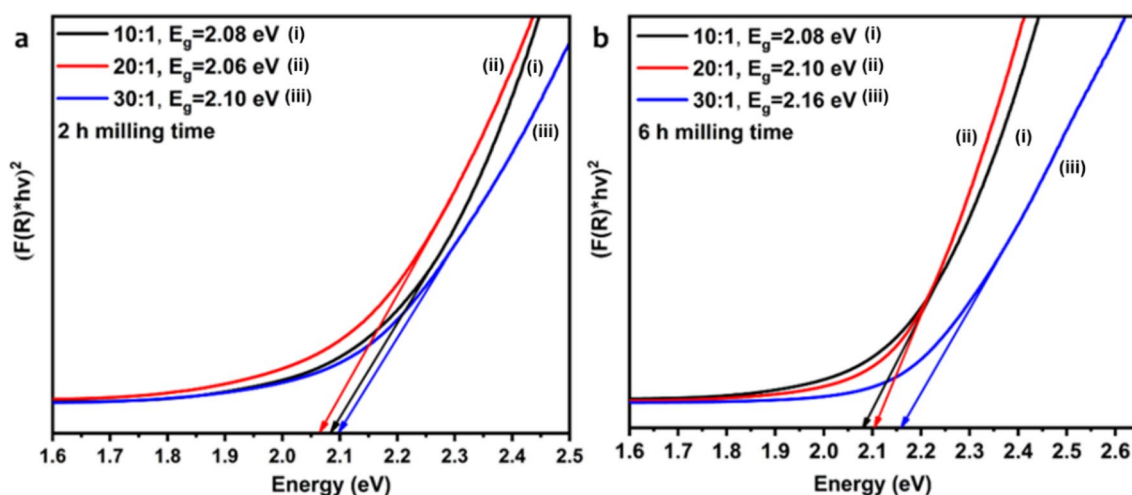


Fig. 5 The bandgap of TiO₂/maghemite composites for different ratios after milling for **a** 2 h and **b** 6 h

Table 4 The average elemental composition of the different ratios milled for 2 and 6 h

BPR	2 h milling		6 h milling	
	%Fe	%Ti	%Fe	%Ti
10:1	46.19	53.81	49.07	50.93
20:1	56.29	43.71	50.14	49.86
30:1	49.61	50.39	47.96	52.04

Raman spectroscopy

Raman spectroscopy is an effective and sensitive technique for studying nanoscale materials based on their crystallinity and phonon nature. This analysis allows us to identify the vibrational, rotational, and other modes, probing the

composition and phase transitions in complex/composite samples [15, 43].

The Raman spectra for the NCs milled for 2 h with BPR of 10:1 (Fig. 6a) showed a broad peak centered at 153.6 cm⁻¹, corresponding to the E_g vibrational mode of TiO₂ anatase phase [44], and smaller peaks at 195.6 cm⁻¹ belonging to the γ-Fe₂O₃ phase [45]. The spectra for BPR of 20:1 showed the increased intensity of γ-Fe₂O₃ vibrational mode with a broad peak at 192.2 cm⁻¹ and a small peak position at 219.7 cm⁻¹ attributed to the presence of hematite phase. The changes in peak intensities could be due to the transformation in the composition, structure, and crystallinity of the material [46], similar to the XRD pattern observations. As described earlier (Sect. 2.1), increasing the BPR causes an associated increase in heat content during milling and can account for the alterations of the peak positions with

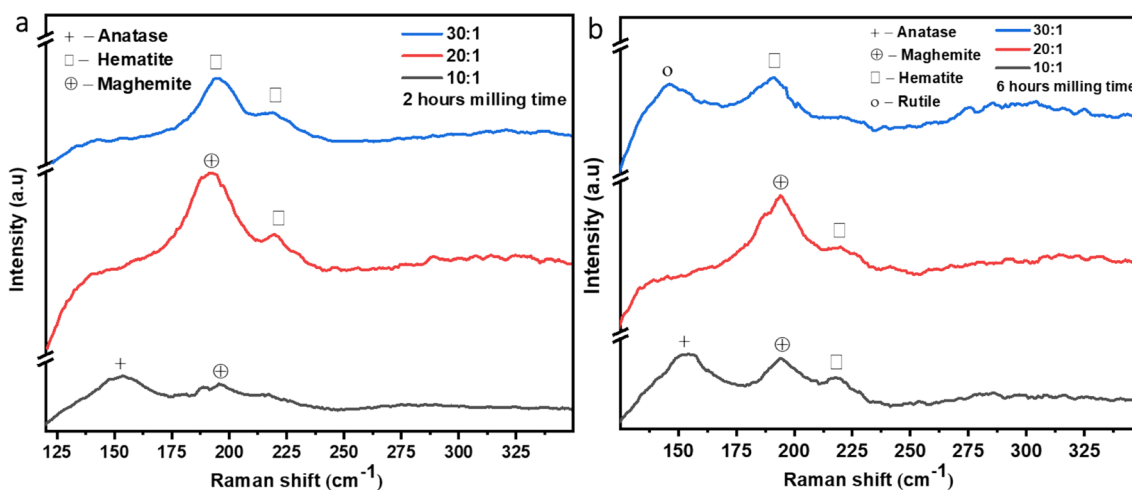


Fig. 6 Raman spectra of TiO₂/maghemite composites for different ratios after milling for **a** 2 h and **b** 6 h

the structure and composition. Further increase in BPR at 30:1 showed decreased peak intensity of the γ -Fe₂O₃ vibration mode and a shoulder peak at 218.9 cm⁻¹, corresponding to hematite. Therefore, an increase in BPR increased the γ -Fe₂O₃ phase peaks with a reduction and apparent disappearance of the anatase TiO₂ vibration mode peaks.

The Raman spectra for the different BPR millings at 6 h (Fig. 6b) showed broad peaks at 152.0 cm⁻¹, which corresponds to the anatase vibrations. It also depicts, with vibration mode for γ -Fe₂O₃ at 193.9 cm⁻¹, a small peak at 218.1 cm⁻¹, due to the hematite phase, as observed in XRD characterization. Further increase in the BPR (20:1) showed an increased intensity of peaks belonging to γ -Fe₂O₃ vibrations (193.9 cm⁻¹) and the disappearance of peak positions for anatase TiO₂. The peaks corresponding to hematite (219.7 cm⁻¹) suggest γ -Fe₂O₃ converting to the hematite phase with increased BPR. Milling with a BPR of 30:1 caused a total change from TiO₂ anatase into rutile phase evidenced by the B_{1g} vibration mode at 146.1 cm⁻¹ [47], mostly in the 6 h-30:1 sample, and the presence of hematite vibration modes at 191.4 cm⁻¹. These observations are similar to that of XRD diffractograms due to reactive heating accompanying the longer milling durations. These spectra support the observations from XRD that milling with a BPR of 10:1 for 2 h or 6 h maintains both anatase

and γ -Fe₂O₃ phases, while higher BPR produces the phase transformations.

SEM analysis

To study the grain shapes and the size distribution of the nanomaterials, SEM analysis was carried out. The SEM image, mapping, and EDS for T/M NCs (10:1–2 and 6 h) are represented in Fig. 7a–f. Figure 7a, b shows the presence of nearly spherical shaped nanoparticles with aggregation between adjacent particles which is due to attractive van der Waals force occurring commonly during the synthesis and process of NCs [48]. The NCs were smaller in size in both the cases and thus possessed a higher relative surface area [49]. Figure 7c, d depicts the homogeneously distributed iron (Fe) and titanium (Ti) elements. The homogeneity is further confirmed from the elemental composition graph from Fig. 7e, f. The EDS spectrum of T/M NCs (10:1) with the atomic composition of Fe and Ti was found to be 46.19 and 53.81% (2 h) and 49.07 and 50.93% (6 h), respectively, which is very close to the desired stoichiometry for ball milling process. The average elemental composition of all the samples is shown in Table 3. The samples for SEM analysis were chosen based on the XRD and Raman analysis results considering no secondary phases.

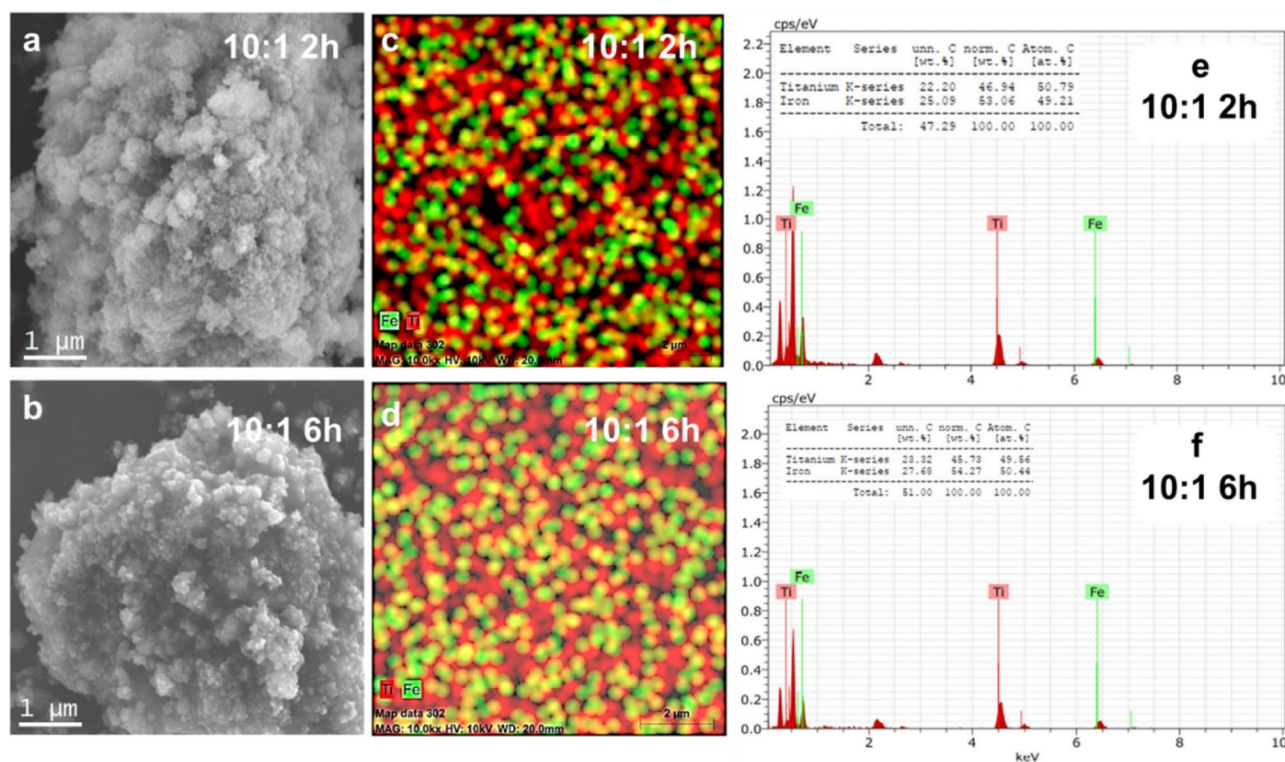


Fig. 7 SEM images, elemental mapping and compositions of ball-milled T/M NCs (10:1 2 and 6 h)

TEM analysis

NCs synthesized using a BPR of 10:1 for 2 h showed the presence of spherical shaped nanoparticles [50] from the TEM micrograph, with the particle sizes ranging from 12 to 25 nm (Fig. 8a). The SAED analysis of atomic arrangements [51] (Fig. 8b) of both Fe and Ti verifies the fringes' observations and confirms the presence of both phases in the nanocomposite. The d-spacing of the image (Fig. 8ci, ii) were measured using an inverse Fast Fourier Transform (FFT) shows fringes of sizes 0.35 nm and 0.25 nm, corresponding to the prominent (101) peaks of anatase TiO_2 and (311) cubic $\gamma\text{-Fe}_2\text{O}_3$ phases, reported from XRD measurements (Table 1).

XPS studies

XPS spectra presented information on the binding energy (BE) of the synthesized anatase- TiO_2 and $\gamma\text{-Fe}_2\text{O}_3$ nano-materials and prepared T/M NCs. The spectra, recorded

with monochromatic Al K_{α} radiation and shown in Fig. 9 contain the core level lines originating from Ti (Ti 2s, Ti 2p), Fe (Fe 2p), and O (O 1s). Figure 9a shows the presence of the T2s photoelectron spectrum at 565 eV, and the T2p peaks at 458 and 464 eV, corresponding to $\text{Ti}2p_{3/2}$ and $\text{Ti}2p_{1/2}$. The difference between the two peaks (ΔBE) is 6 eV, which is characteristic of Ti(IV) ions [52]. The Fe 2p spectrum shows two BE peaks at 710 eV and 723.5 eV, corresponding to $\text{Fe}2p_{3/2}$ and $\text{Fe}2p_{1/2}$. The difference between the two peaks (ΔBE) is 13.5 eV, which is the characteristic of Fe(III) ions present in maghemite [53].

Spectral analysis of the T/M composites synthesized with a BPR of 10:1 for 2 h has a ΔBE between Ti $2p_{1/2}$ (463 eV) and Ti $2p_{3/2}$ (468 eV) of ~ 5 eV. Similarly, ΔBE between Ti $2p_{1/2}$ (460 eV) and Ti $2p_{3/2}$ (465 eV) for 6 h synthesis is ~ 5 eV (Fig. 9b), which is lesser than the value of the only TiO_2 . The decrease in ΔBE for Ti(IV) provides indirect evidence of forming the chemical Ti–O–Fe interfacial bond. The internal electric field promotes the

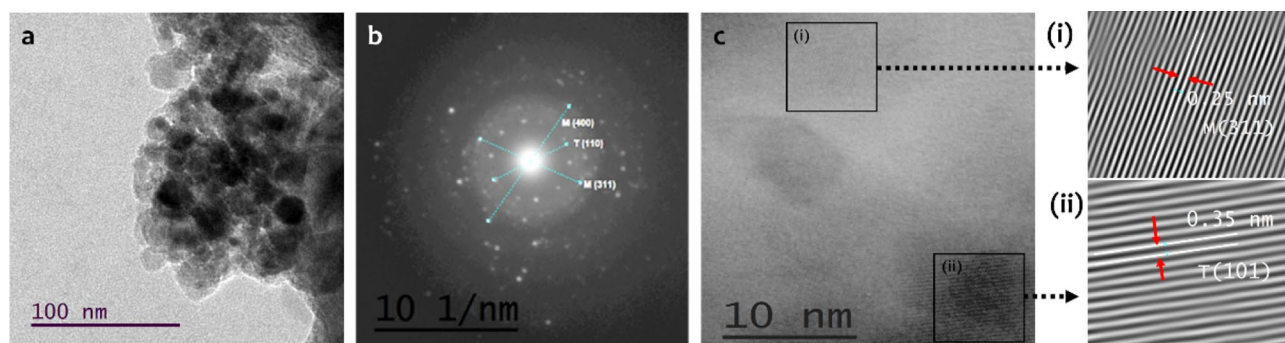


Fig. 8 HRTEM micrographs of sample T/M NCs with a BPR of 10:1 for 2 h showing the **a** particle size distribution, **b** SAED pattern, **c** fringes corresponding to inter-planar spacing. (i) Fe and (ii) Ti

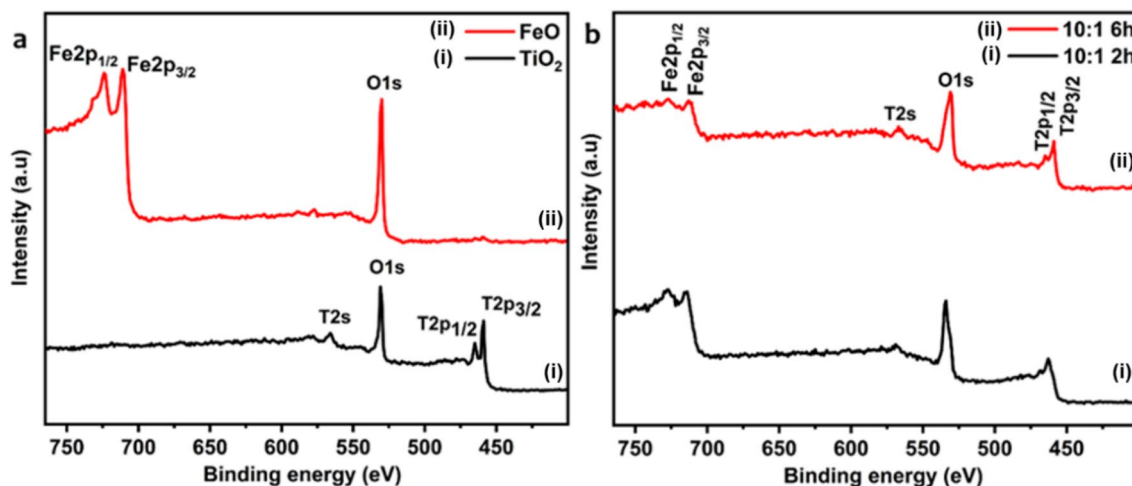


Fig. 9 XPS spectra for **a** synthesized TiO_2 and maghemite nanostructures, and **b** T/M composites with BPR of 10:1 for 2 and 6 h milling

transfer of electrons from Fe_2O_3 to TiO_2 , responsible for the observed reduction in the NCs bandgap [54, 55].

The O 1 s spectrum of TiO_2 and FeO appear at 530 eV, corresponding to lattice oxygen and O–H bond, and the presence of H in the bond may be due to brief exposure to the ambience. However, in the NCs, the BE of the O–H bond is less than that in TiO_2 , which further supports the formation of the Ti–O–Fe bond in the nanocomposite [56].

Adsorption evaluation studies

From UV–Vis results, the formation of T/M NCs causes the electron transfer (e^-) from $\gamma\text{-Fe}_2\text{O}_3$ to TiO_2 , leaving the $\gamma\text{-Fe}_2\text{O}_3$ with an equal amount of holes (e^+) [57] and thereby reducing the bandgap of the T/M nanomaterials (Sect. 2.3.1). During the water treatment, the TiO_2 material releases an e^- with an equivalent number of e^+ donated from the $\gamma\text{-Fe}_2\text{O}_3$ material. Thus, the charges which participate in the adsorption mechanisms are available without the need for an external source, sunlight, and can proceed in the dark too. The adsorption mechanism for As species in the presence of charges may take place in the following steps [38]:

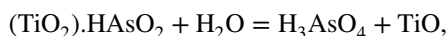
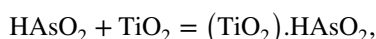
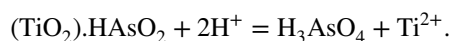


Table 5 The average As(III) and (V) removal percentage for TiO_2 and $\gamma\text{-Fe}_2\text{O}_3$

Samples	As(III) % Av. removal	As(V) % Av. removal
TiO_2 Anatase	26.37	17.65
Maghemite	38.41	25.14



A constant dosage of 0.5 g/L and a pH of 7.0 was used for the adsorption studies, with 2 ppm concentration in ambient temperature for 5 min. The average percentage of As(III) and (V) removal (Table 5) for as-synthesized $\gamma\text{-Fe}_2\text{O}_3$ and TiO_2 , with maghemite showing more %removal than TiO_2 , may be due to the comparative and presence of excess free e^- in $\gamma\text{-Fe}_2\text{O}_3$ as the processes were carried out in the dark. The average adsorption for As(III) using the different T/M NCs ratios synthesized for 2 h and 6 h (Fig. 10) is indirectly proportional to the performance as the BPR increases.

The percentage removal for T/M NC synthesis with BPR 10:1 for 2 h (Fig. 10a) shows a better performance in As(III) removal with an average value of 50%. In the case of 20:1 BPR, which appears to have a lower bandgap with a larger crystallite size, may affect the effective surface area resulting in lesser adsorption. A further decline in the performance of 30:1 BPR may be attributed to the decrease in phase content, an even lower (I_{101}/I_{311}) intensity ratio, and observed bandgap increment. The T/M NCs synthesized for 6 h (Fig. 10b) showed a similar trend in declining performance with increasing BPR due to the synthesized nanomaterials' properties. A comparison of As(III) removal shows that NCs milled for 6 h appear to have a comparatively better performance than the 2 h counterparts. This relative improvement in performance could be due to their smaller crystallite size, leading to more crystallites in a given volume and a larger surface area [58].

The adsorption processes for removing As(V) using the NCs in both 2 h and 6 h (Fig. 11) showed reduced

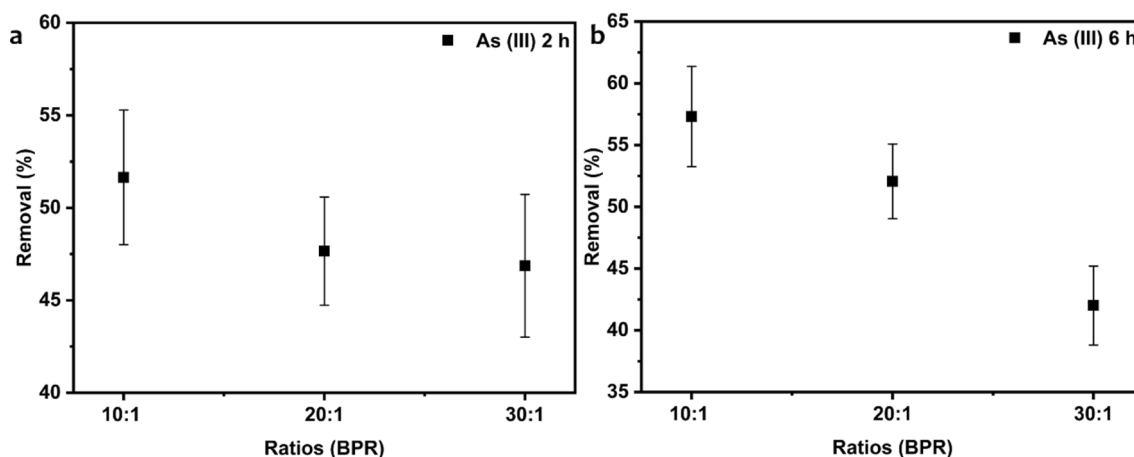


Fig. 10 The removal % of As(III) with different BPR ratios **a** 2 h and **b** 6 h milling



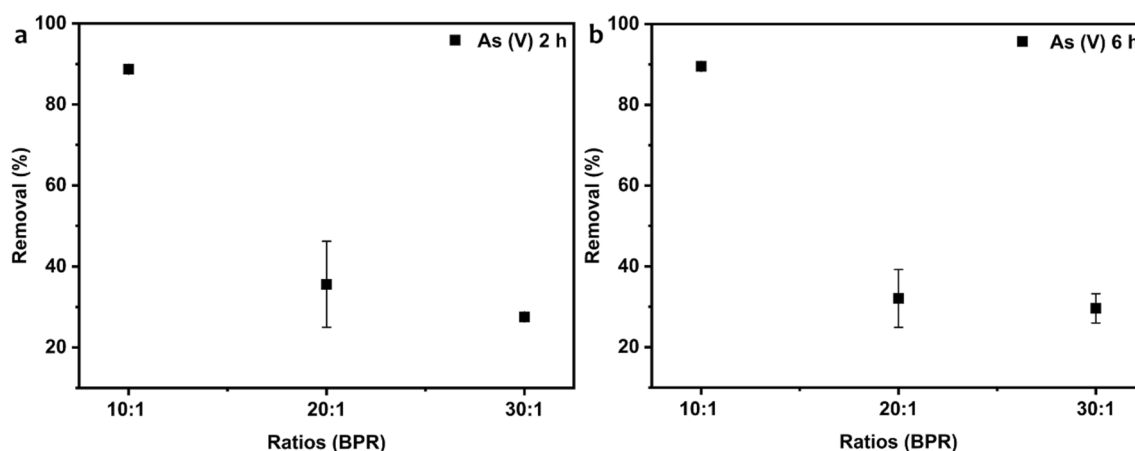


Fig. 11 The removal % of As(V) with different BPR ratios **a** 2 h and **b** 6 h milling

performances with increasing BPR. The T/M NCs with BPR 10:1 show ~90% removal of the As(V) contaminants, which decreases with an increase in BPR ratios for both durations. Since both NCs show similar performance with BPR 10:1 (2 and 6 h), an optimum time of 2 h could be employed to scaling-up the synthesis for industrial applications for As(V) removal. We carried out the adsorption processes for only 5 min to verify the viability of materials synthesized using ball milling and optimizing the milling parameters in removing both As(III) and As(V). The next phase of the study will be focused on modulating other parameters (e.g., pH, temperature, dosage, concentration) and allowing a longer duration for the adsorption process.

Conclusion

A successful synthesis of TiO₂ and γ -Fe₂O₃ nanocomposite structures using the facile ball-milling technique by optimizing the BPR and milling time was used to adsorb As(III) and (V). Synthesis with a BPR of 10:1 for both 2 and 6 h showed the presence of desired anatase and maghemite phases with the most intense peak ratio above 1.2, showing desirable performance in arsenic removal. Electron microscopy studies on samples synthesized with a 10:1 for both 2 h presented particle shapes corresponding to anatase TiO₂ phase. The T/M nanocomposites' bandgaps showed some modifications, ranging from 2.06 to 2.16 eV, depicting the transfer of electrons from γ -Fe₂O₃ to the TiO₂ material, supported by XPS characterization. Studies using Raman spectroscopy for the vibration modes confirmed the structure's anatase and maghemite phases' presence and their respective transformations.

Adsorption studies showed above 50% removal of As(III) and ~90% performance in the removal of As(V) using nanomaterials synthesized using a BPR of 10:1 for both 2 and 6 h, respectively. The performance confirms that the ball

milling technique can produce nanomaterials with desirable properties for adsorption purposes. Further studies will focus on optimizing other parameters and permitting a more extended duration that affects the adsorption process to achieve the recommended permissible concentration of arsenic in water bodies.

Acknowledgements The authors are thankful to Consejo Nacional de Ciencia y Tecnología (National Council of Science and Technology, CONACyT-Mexico) for providing the financial support from the project CONACyT-SENER 263043.

Author contribution Mercyrani Babudurai: Carried out experiments, Methodology, conceptualization, writing – original draft, consolidating results. Onyekachi Nwakanma: Formal analysis and writing – contributing to original draft. Araceli Romero-Nuñez: interpretations, data preparation, review. Ravichandran Manisekaran: Writing, review and editing, data curation. Homero Castaneda: Guidance, Revision, Validation, draft formatting. Anish Jantrania: Help in experimental results interpretations, advice to improve draft, format corrections. Velumani Subramaniam: Supervision, resource, project administration.

References

- Shaji, E., Santosh, M., Sarath, K.V., Prakash, P., Deepchand, V., Divya, B.V.: Arsenic contamination of groundwater: a global synopsis with focus on the Indian Peninsula. *Geosci. Front.* (2020). <https://doi.org/10.1016/j.gsf.2020.08.015>
- Gomes, J.A., Rahman, M.S., Das, K., Varma, S., Cocke, D.: A comparative electrochemical study on arsenic removal using iron, aluminum, and copper electrodes. *ECS Trans.* **25**, 59–68 (2019)
- Saha, R., Dey, N.C., Rahman, M., Bhattacharya, P., Rabbani, G.H.: Geogenic arsenic and microbial contamination in drinking water sources: exposure risks to the coastal population in Bangladesh. *Front. Environ. Sci.* **7**, 57 (2019)
- Sinha, D., Prasad, P.: Health effects inflicted by chronic low-level arsenic contamination in groundwater: a global public health challenge. *J. Appl. Toxicol.* **40**, 87–131 (2020)
- Qa, M., Ms, K.: Effect on human health due to drinking water contaminated with heavy metals. *J. Pollut. Eff. Control* **05**, 10–11 (2016)

6. Lata, S., Samadder, S.R.: Removal of arsenic from water using nano adsorbents and challenges: a review. *J. Environ. Manag.* **166**, 387–406 (2016)
7. Kabir, F., Chowdhury, S.: Arsenic removal methods for drinking water in the developing countries: technological developments and research needs. *Environ. Sci. Pollut. Res.* **24**, 24102–24120 (2017)
8. Çermikli, E., Şen, F., Altıok, E., Wolska, J., Cyganowski, P., Kabay, N., Bryjak, M., Arda, M., Yüksel, M.: Performances of novel chelating ion exchange resins for boron and arsenic removal from saline geothermal water using adsorption-membrane filtration hybrid process. *Desalination* **491**, 114504 (2020)
9. Pessoa Lopes, M., Galinha, C.F., Crespo, J.G., Velizarov, S.: Optimisation of arsenate removal from water by an integrated ion-exchange membrane process coupled with Fe co-precipitation. *Sep. Purif. Technol.* **246**, 116894 (2020)
10. Ince, M., Kaplan Ince, O.: An overview of adsorption technique for heavy metal removal from water/wastewater: a critical review. *Int. J. Pure Appl. Sci.* **3**, 10–19 (2017)
11. Siddiqui, S.I., Chaudhry, S.A.: Iron oxide and its modified forms as an adsorbent for arsenic removal: a comprehensive recent advancement. *Process Saf. Environ. Prot.* **111**, 592–626 (2017)
12. La, D., Nguyen, T., Jones, L., Bhosale, S.: Graphene-supported spinel CuFe₂O₄ composites: novel adsorbents for arsenic removal in aqueous media. *Sensors* **17**, 1292–1306 (2017)
13. La, D.D., Patwari, J.M., Jones, L.A., Antolasic, F., Bhosale, S.V.: Fabrication of a GNP/Fe–Mg binary oxide composite for effective removal of arsenic from aqueous solution. *ACS Omega* **2**, 218–226 (2017)
14. Zhou, W., Fu, H., Pan, K., Tian, C., Qu, Y., Lu, P., Sun, C.C.: Mesoporous TiO₂/α-Fe₂O₃: bifunctional composites for effective elimination of arsenite contamination through simultaneous photocatalytic oxidation and adsorption. *J. Phys. Chem. C* **112**, 19584–19589 (2008)
15. Ceballos-Chuc, M.C., Ramos-Castillo, C.M., Alvarado-Gil, J.J., Oskam, G., Rodríguez-Gattorno, G.: Influence of brookite impurities on the raman spectrum of TiO₂ anatase nanocrystals. *J. Phys. Chem. C* **122**, 19921–19930 (2018)
16. La, D.D., Thi, H.P.N., Nguyen, T.A., Bhosale, S.V.: Effective removal of Pb(II) using a graphene@ternary oxides composite as an adsorbent in aqueous media. *New J. Chem.* **41**, 14627–14634 (2017)
17. Ahamed, S., Hussam, A., Munir, A.K.M.: Groundwater arsenic removal technologies based on sorbents. In: Ahuja, S. (ed.) *Handbook of Water Purity and Quality*, pp. 379–417. Elsevier, USA (2009)
18. Kelly, S.D.: Uranium chemistry in soils and sediments. In: *Developments in Soil Science*. Elsevier **34**, 411–466 (2010). [https://doi.org/10.1016/S0166-2481\(10\)34014-1](https://doi.org/10.1016/S0166-2481(10)34014-1)
19. Miao, J., Zhang, R., Zhang, L.: Photocatalytic degradations of three dyes with different chemical structures using ball-milled TiO₂. *Mater. Res. Bull.* **97**, 109–114 (2018)
20. Han, Q., Setchi, R., Evans, S.L.: Synthesis and characterisation of advanced ball-milled Al–Al₂O₃ nanocomposites for selective laser melting. *Powder Technol.* **297**, 183–192 (2016)
21. Bui, T.T., Le, X.Q., To, D.P., Nguyen, V.T.: Investigation of typical properties of nanocrystalline iron powders prepared by ball milling techniques. *Adv. Nat. Sci. Nanosci. Nanotechnol.* **4**, 045003–045012 (2013)
22. El-sheerif, R.M., Lasheen, T.A., Jebriil, E.A.: Fabrication and characterization of CeO₂–TiO₂–Fe₂O₃ magnetic nanoparticles for rapid removal of uranium ions from industrial waste solutions. *J. Mol. Liq.* **241**, 260–269 (2017)
23. Jamkhande, P.G., Ghule, N.W., Bamer, A.H., Kalaskar, M.G.: Metal nanoparticles synthesis: an overview on methods of preparation, advantages and disadvantages, and applications. *J. Drug Deliv. Sci. Technol.* **53**, 101174 (2019)
24. Castrillón Arango, J.A., Cristóbal, A.A., Ramos, C.P., Bercoff, P.G., Botta, P.M.: Mechanochemical synthesis and characterization of nanocrystalline Ni_{1-x}Co_xFe₂O₄ (0 ≤ x ≤ 1) ferrites. *J. Alloys Compd.* **811**, 152044 (2019)
25. Hu, J., Geng, X., Duan, Y., Zhao, W., Zhu, M., Ren, S.: Effect of mechanical–chemical modification process on mercury removal of bromine modified fly ash. *Energy Fuels* **34**, 9829–9839 (2020)
26. Jiang, J., Li, J.: Mechanically induced N-arylation of amines with diaryliodonium salts. *ChemistrySelect* **5**, 542–548 (2020)
27. Do, J.L., Friščić, T.: Mechanochemistry: a force of synthesis. *ACS Cent. Sci.* **3**, 13–19 (2017)
28. Zhu, Y., Zhang, L.I., Gao, C., Cao, L.: The synthesis of nanosized TiO₂ powder using a sol-gel method with TiCl₄ as a precursor. *J. Mater. Sci.* **35**, 4049–4054 (2000)
29. Mercyrani, B., Hernandez-Maya, R., Solís-López, M., Th-Th, C., Velumani, S.: Photocatalytic degradation of Orange G using TiO₂/Fe₃O₄ nanocomposites. *J. Mater. Sci. Mater. Electron.* **29**, 15436–15444 (2018)
30. Deepa, K., Himagirish Kumar, S., Paul Raj, Y., Jyothi, N.V.V., Lingappa, Y.: A simple spectrophotometric method for the determination of arsenic in industrial and environmental samples using vanillin-2-amino nicotinic acid (VANA). *Der. Pharm. Lett.* **7**, 345–352 (2015)
31. Naguib, I.A., Abdelaleem, E.A., Hassan, E.S., Emam, A.A.: Comparative study of eco-friendly spectrophotometric methods for accurate quantification of mebendazole and quinamide combination; content uniformity evaluation. *Spectrochim. Acta Part A Mol. Biomol. Spectrosc.* **235**, 118271 (2020)
32. Shahat, A., Hassan, H.M.A., Azzazy, H.M.E., Hosni, M., Awual, M.R.: Novel nano-conjugate materials for effective arsenic(V) and phosphate capturing in aqueous media. *Chem. Eng. J.* **331**, 54–63 (2018)
33. Morán, A., Nwakanma, O., Velumani, S., Castaneda, H.: Comparative study of optimised molybdenum back-contact deposition with different barriers (Ti, ZnO) on stainless steel substrate for flexible solar cell application. *J. Mater. Sci. Mater. Electron.* **31**, 7524–7538 (2020)
34. Makuła, P., Pacia, M., Macyk, W.: How to correctly determine the band gap energy of modified semiconductor photocatalysts based on UV–Vis spectra. *J. Phys. Chem. Lett.* **9**, 6814–6817 (2018)
35. Khot, A.C., Desai, N.D., Khot, K.V., Salunkhe, M.M., Chougule, M.A., Bhawe, T.M., Kamat, R.K., Musselman, K.P., Dongale, T.D.: Bipolar resistive switching and memristive properties of hydrothermally synthesized TiO₂ nanorod array: effect of growth temperature. *Mater. Des.* **151**, 37–47 (2018)
36. Mariño-Salguero, J., Jorge, J., Menéndez-Aguado, J.M., Álvarez-Rodríguez, B., De Felipe, J.J.: Heat generation model in the ball-milling process of a tantalum ore. *Miner. Metall. Process.* **34**, 10–19 (2017)
37. Suryanarayana, C., Ivanov, E., Noufi, R., Contreras, M.A., Moore, J.J.: Phase selection in a mechanically alloyed Cu–In–Ga–Se powder mixture. *J. Mater. Res.* **14**, 377–383 (1999)
38. Oscarson, D.W., Huang, P.M., Hammer, U.T., Liaw, W.K.: Oxidation and sorption of arsenite by manganese dioxide as influenced by surface coatings of iron and aluminum oxides and calcium carbonate. *Water. Air. Soil Pollut.* **20**, 233–244 (1983)
39. Danish, M.I., Qazi, I.A., Zeb, A., Habib, A., Awan, M.A., Khan, Z.: Arsenic removal from aqueous solution using pure and metal-doped Titania nanoparticles coated on glass beads: adsorption and column studies. *J. Nanomater.* **2013**, 1–17 (2013)
40. Mohan, D., Pittman, C.U.: Arsenic removal from water/wastewater using adsorbents—a critical review. *J. Hazard. Mater.* **142**, 1–53 (2007)



41. Awual, M.R., Shenashen, M.A., Yaita, T., Shiwaku, H., Jyo, A.: Efficient arsenic(V) removal from water by ligand exchange fibrous adsorbent. *Water Res.* **46**, 5541–5550 (2012)
42. Xia, C., Jia, Y., Tao, M., Zhang, Q.: Tuning the band gap of hematite α -Fe₂O₃ by sulfur doping. *Phys. Lett. Sect. A Gen. At. Solid State Phys.* **377**, 1943–1947 (2013)
43. Niewiadomski, A., Kania, A., Kugel, G.E., Hafid, M., Sitko, D.: Raman spectroscopy, dielectric properties and phase transitions of Ag_{0.96}Li_{0.04}NbO₃ ceramics. *Mater. Res. Bull.* **65**, 123–131 (2015)
44. Stagi, L., Carbonaro, C.M., Corpino, R., Chiriu, D., Ricci, P.C.: Light induced TiO₂ phase transformation: correlation with luminescent surface defects. *Phys. Status Solidi Basic Res.* **252**, 124–129 (2015)
45. Skvortsova, V.L., Samoylovich, M.I., Belyanin, A.F.: Studies of phase composition of contact sites of diamond crystals and the surrounding rocks. *Dokl. Earth Sci.* **465**, 1187–1190 (2015)
46. Rezaee, M., Mousavi Khoie, S.M., Liu, K.H.: The role of brookite in mechanical activation of anatase-to-rutile transformation of nanocrystalline TiO₂: an XRD and Raman spectroscopy investigation. *CrystEngComm* **13**, 5055–5061 (2011)
47. Challagulla, S., Tarafder, K., Ganesan, R., Roy, S.: Structure sensitive photocatalytic reduction of nitroarenes over TiO₂. *Sci. Rep.* **7**, 1–11 (2017)
48. Deng, X., Huang, Z., Wang, W., Davé, R.N.: Investigation of nanoparticle agglomerates properties using Monte Carlo simulations. *Adv. Powder Technol.* **27**, 1971–1979 (2016)
49. Rahman, M.T., Asadul Hoque, M., Rahman, G.T., Gafur, M.A., Khan, R.A., Hossain, M.K.: Study on the mechanical, electrical and optical properties of metal-oxide nanoparticles dispersed unsaturated polyester resin nanocomposites. *Results Phys.* **13**, 102264 (2019)
50. Li, C.Y., Wang, J.B., Wang, Y.Q.: Microstructure and photocatalytic activity of titanium dioxide nanoparticles. *Chin. Phys. B* **21**, 1–5 (2012)
51. Liu, J., Meeprasert, J., Namuangruk, S., Zha, K., Li, H., Huang, L., Maitarad, P., Shi, L., Zhang, D.: Facet-activity relationship of TiO₂ in Fe₂O₃/TiO₂ nanocatalysts for selective catalytic reduction of NO with NH₃. In situ DRIFTS and DFT studies. *J. Phys. Chem. C* **121**, 4970–4979 (2017)
52. Zhang, X., Zhou, J., Gu, Y., Fan, D.: Visible-light photocatalytic activity of N-doped TiO₂ nanotube arrays on acephate degradation. *J. Nanomater.* **2015**, 1–6 (2015)
53. Radu, T., Iacovita, C., Benea, D., Turcu, R.: X-ray photoelectron spectroscopic characterization of iron oxide nanoparticles. *Appl. Surf. Sci.* **405**, 337–343 (2017)
54. Briggs, D.: X. In: Packham, D. E. (ed.) *Handbook of Adhesion*, pp. 621–622. John Wiley & Sons, Ltd, Chichester, UK (2005)
55. Yan, J., Zhang, Y., Liu, S., Wu, G., Li, L., Guan, N.: Facile synthesis of an iron doped rutile TiO₂ photocatalyst for enhanced visible-light-driven water oxidation. *J. Mater. Chem. A* **3**, 21434–21438 (2015)
56. Akhavan, O.: Thickness dependent activity of nanostructured TiO₂/ α -Fe₂O₃ photocatalyst thin films. *Appl. Surf. Sci.* **257**, 1724–1728 (2010)
57. Nayak, M.K., Singh, J., Singh, B., Soni, S., Pandey, V.S., Tyagi, S.: Introduction to semiconductor nanomaterial and its optical and electronics properties. In: Gupta, R.K., Misra, M. (eds.) *Metal Semiconductor Core-Shell Nanostructures for Energy and Environmental Applications*, pp. 1–33. Elsevier (2017)
58. Bueno-Ferrer, C., Parres-Esclapez, S., Lozano-Castelló, D., Bueno-López, A.: Relationship between surface area and crystal size of pure and doped cerium oxides. *J. Rare Earths.* **28**, 647–653 (2010)

Publisher's Note Springer Nature remains neutral with regard to jurisdictional claims in published maps and institutional affiliations.

